On the asymmetric vortex evolution in the near wake behind polygonal cylinders in an incident flow

Hao Cheng[a,b,c], Esmaeel Masoudi[c], Yu Liu[a,*], Lian Gan[c,*]

[a]*Department of Mechanics and Aerospace Engineering, Southern University of Science and Technology, Shenzhen 518055, China,*
[b]*Department of Aerospace and Mechanical Engineering, University of Southern California, Los Angeles, California, 90089, USA,*
[c]*Department of Engineering, Durham University, Durham, DH1 3LE, United Kingdom,*

Abstract

Asymmetric evolution of coherent vortices behind polygonal cylinders in an incident flow is studied using Proper Orthogonal Decomposition (POD) based phase averaging analysis. Flow around polygonal cylinders of side number $N \in [5,8]$ at Reynolds number 10^4 is simulated using three-dimensional Large Eddy Simulation for six incident angles α to cover the entire incidence spectrum. POD analysis is performed on a two-dimensional subset of the data at the mid-span of the cylinder. It is found that except heptagon at corner orientation, where extra secondary vortex shedding is observed, all the other cases resemble the classical periodic Kármán vortex shedding at the Strouhal frequency. The first pair of POD eigenvalues show similar and dominant energy content in all the cases, with negligible N or α dependence. Maximum circulation of primary vortices calculated using the POD-based phase averaging method displays significant asymmetry between the vortices shed on the upper and lower sides, when the cylinder is at off-principal orientations with respect to the incoming flow. This maximum circulation on each side of the wake occurs close to a properly defined vortex formation distance where vortex centroids are closest apart in the transverse direction. Correlation analysis reveals that the difference of the maximum circulations between the upper and lower sides scales weakly with the time-mean lift coefficient, and their sum scales well with the time-mean drag coefficient positively and Strouhal number inversely.

Keywords: polygonal cylinder, incident flow, POD, coherent vortex evolution

1. Introduction

Polygonal cylinders, which refer to cylinders of polygonal cross-sectional shapes, are widely seen in architectural and engineering applications. Fluid mechanical characteristics associated with polygonal cylinders, such as oscillatory aerodynamic forces and periodic wake flows, typically resemble those of general two-dimensional bluff-bodies, e.g., the circular cylinder. Specifically, the periodic vortex shedding with a certain frequency causes vibration on the objects, that is, the so-called vortex-induced vibration (VIV), frequently occurs in ocean engineering applications[1, 2], such as in the design and stability analysis of offshore platforms, marine structures, marine risers, and underwater vehicles. Flow around polygonal cylinders of different side numbers N, at various incoming flow incidence angles α (because of their quasi-axisymmetric geometries) and Reynolds numbers Re, manifests distinct flow separation characteristics, and hence the induced fluid forces and wake evolution. In particular, it was previously shown in a systematic wind tunnel experiment [3] for cylinders of $N \in [2,16]$ at principal orientations (either a flat surface or an edge facing normally to the incoming flow) that lift and drag forces as well as the Strouhal number, St, all exhibit significant non-linear dependence on N. Flow past those polygonal cylinders in general resembles the one past the circular cylinder [3]. However, unlike the continuous surface of a circular cylinder, their geometrical discontinuity largely determines the location of flow separation points, and hence the topology of the near wake flow region. For a

*Corresponding author
Email addresses: hcheng85@usc.edu (Hao Cheng), esmaeel.masoudi@durham.ac.uk (Esmaeel Masoudi), liuy@sustech.edu.cn (Yu Liu), lian.gan@durham.ac.uk (Lian Gan)

polygonal cylinder of $N \lesssim 10$, flow tends to separate at a fixed edge, showing weak sensitivity to Re in the sub-critical regime [4]. It thus can be expected that at an arbitrary (off-principal) orientation, there exists subtle variation on α of the aerodynamic forces, including a non-zero time-mean lift, which indeed is confirmed by a recent Large Eddy Simulation (LES) study for polygonal cylinders of $N \in [5,8]$ covering the entire α spectrum [5].

In terms of the flow characteristics in the wake behind polygonal cylinders, those for the triangular ($N = 3$) and the square cylinder ($N = 4$) have been extensively studied owing to their simple geometry and wide applications. To mention a few among others, Agrwal *et al.* [6] experimentally studied the effect of the apex angle on the flow around the triangular cylinder using Particle Image Velocimetry (PIV) at $\mathrm{Re} = 520$, focusing on the flow structure and aerodynamic forces. It was found that the drag coefficient C_D increases with the apex angle, while St is inversely proportional to the apex angle. The results of turbulence intensity and the spanwise vorticity showed that as the apex angle increases, vortex shedding is delayed, and the recirculation region behind the cylinder is extended further into the wake. In addition, the power spectra density (PSD) from the velocity signal, measured using hot-wire anemometer showed additional peaks other than the Strauhal frequency in the frequency spectrum, attributed to the non-linear interaction between the Kármán vortices from the upper and the lower side. Lyn *et al.* [7] investigated the flow around a square cylinder in turbulent regime using two-component Laser Doppler Velocimetry measurements and phase averaging based on the pressure signal. They found that the streamwise evolution of the circulation of coherent vortices in the near wake region is very similar to that of the circular cylinder. The average decay rate of circulation is slightly larger than that of the circular cylinder. They also found that the maximum circulation of these vortices is about 60% higher than that of the circular cylinder, which is attributed to the larger vorticity magnitude and vortex size. Oudheusden *et al.* [8] performed Proper Orthogonal Decomposition (POD) analysis on their PIV data to study the effect of α on the flow features. They reconstructed the turbulent flow field using the first two POD modes having the highest energy content, which is about 75% of the total turbulent kinetic energy. POD provided a good global phase identifier which enables effective investigation of coherent vortex evolution at various α. Hu *et al.* [9] experimentally studied the effect of the corner radius of a square cylinder on the near wake flow using PIV and phase averaging. They found that as the corner radius increases, the peak vorticity and circulation of the coherent vortex structure both decay while the vortex shedding frequency increases significantly. Also, since the vortex shedding frequency grows with increasing corner radius, the wavelength between tandem vortices decreases. Bai and Alam [10] investigated the dependence of wake flow structures, as well as the time-mean C_D for the square and the circular cylinder over the range of $10^3 < \mathrm{Re} < 10^7$ and classified their dependency on Re into five distinctive regimes.

Studies of cylinders with $N \geq 5$ are relatively scarce. Khaledi and Andersson [11] numerically studied the wake behind a hexagonal cylinder ($N = 6$) at corner and face orientation for $10^2 \leq \mathrm{Re} \leq 10^3$, and found that St for the face oriented case is larger than the corner orientation and it increases with Re for $100 \leq \mathrm{Re} \leq 500$. Tian and Wu [12] studied even N polygonal cylinders at corner orientation for both inviscid and low Re viscous flows. Considering the Re effect, they proposed a correction to the linear relation between St and $\mathrm{Re}^{-1/2}$ originally proposed by Fey *et al.* [13]. Yang *et al.* [14] numerically studied the aerodynamic performance and VIV characteristics of an 18-sided polygon cylinder. They examined the influence on C_D of Re for $2.3 \times 10^4 \lesssim \mathrm{Re} \lesssim 10.6 \times 10^4$, and the surface roughness at $\mathrm{Re} = 7.1 \times 10^4$. A significant reduction of in C_D up to 47% has been found in comparison with the circular cylinder. They also found that as the surface roughness increases, the C_D initially decreases, then increases and eventually stabilizes since the separation points are fixed at the edge of the groove at higher roughness values.

The aerodynamic forces and wake flow characteristics on $N \in [2,16]$ for $10^4 \leq \mathrm{Re} \leq 10^5$ were more systematically studied by Xu *et al.* [3] in a wind tunnel, but only for principal orientations. They found that C_D, lift coefficient fluctuation C_L' and St all show strong dependence on N and orientation. A corrected flow separation angle ζ, which takes into consideration the observed separation-reattachment phenomena, was proposed. Correlations for St-ζ and C_D-ζ were presented. Furthermore, the semi-empirical correlation $\zeta = C_D^{0.6}\mathrm{St}$ was proposed. Wang *et al.* [4, 15] addressed the dependence of flow characteristic length scales and the evolution of coherent wake vortices for polygons of $N \geq 3$ at $\mathrm{Re} = 10^4$ using PIV measurements in a wind tunnel. It was found that both C_D and C_L' are linearly correlated with the wake width, supported by two empirical functions. The coherent vortex structure extracted by POD phase analysis suggested a spatially two-stage development of vortex circulation, separated at the vortex formation length, where the circulation maximises. The vortex centroid trajectory showed that vortices shed from the upper and lower side first move towards the wake centerline and then away from it. They also found that the size of the vortices grows monotonically downstream for all the tested cases whose scaled growth rate is almost universal.

Masoudi *et al.* [5, 16] extended the aforementioned studies by considering incidence angle α effect on polygonal

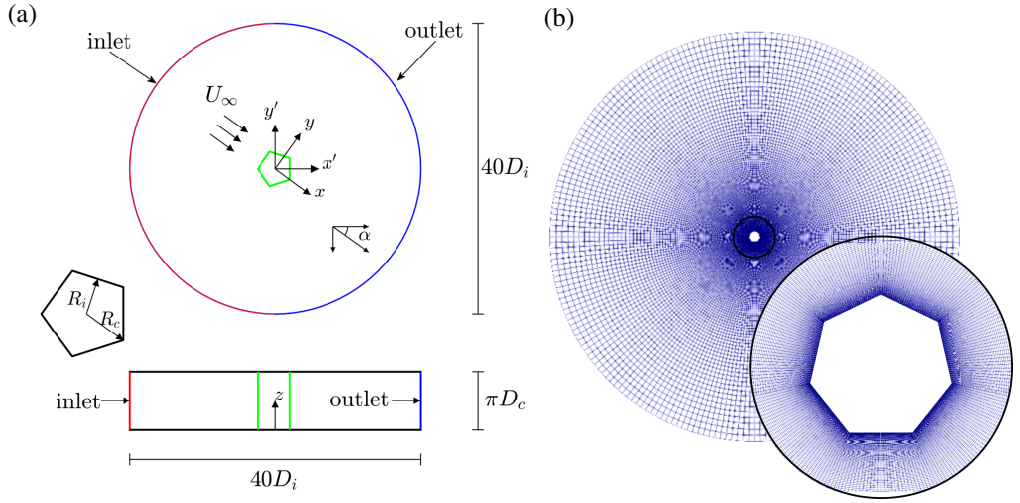

Figure 1: (a) Schematic of the computational domain and problem configuration (not to scale); (b) Global mesh (x-y plane view) of Heptagonal cylinder, with a close-up view of the mesh near the cylinder surface at the bottom right [18].

cylinders of $N \in [5,8]$ using LES at $\mathrm{Re} = 10^4$. In addition to the aerodynamic forces and time-mean wake flow, they noticed a flapping motion associated with separated shear layers, whose strength varies non-linearly with N and α, which affects the shear layer reattachment and secondary separation behaviour. This flapping motion correlates directly with C_D and St, and indirectly with the time-mean lift coefficient C_L. Furthermore, since the flapping motion leaves clear footprint in the time-mean shear layer topology, empirical formulations based on the time-mean shear layer length and width were proposed, which unify C_D, C_L and St for the polygonal cylinder studied, as well as those not studied but available in the literature [3, 4], including the circular cylinder. The classical inverse relationship between C_D and St [3, 17] was also confirmed for arbitrary α conditions.

To the best of our knowledge, the asymmetric evolution of the coherent vortices shed behind these cylinders and their relations to the characteristic aerodynamic behaviours, owing to the effect of the incidence angle α, are yet to be revealed. In this work, we aim to directly address this, making use of the available LES data in Masoudi *et al.* [5] POD is applied as the flow field phase identifier to extract phase-averaged flow fields. The Re studied in the current study is within the sub-critical regime where no transition phenomena have been observed in experiment [3], due to the small side number of the polygons studied. Primary flow separation points are fixed at two corners and insensitive of Re. Therefore the results obtained in this study are expected to be valid across a wide sub-critical Re regime.

2. Methodology

2.1. Computational modelling and numerical setup

Three-dimensional constant Smagorinsky LES was implemented in OpenFOAM and performed on polygonal cylinders of $N \in [5,8]$, each at six equal-spaced incidence angles α. Based on the dimensionless incidence angle, defined as $\alpha^* = \alpha N/180^\circ$, the equal space $\Delta\alpha^* = 0.2$. $\alpha^* = 0$ and 1 are defined for the corner and the face orientation, respectively. $\mathrm{Re} = U_\infty D_i/\nu = 1.0 \times 10^4$, where U_∞ is the free stream velocity, D_i is the in-circle diameter of the cylinder and ν is the kinematic viscosity of the working fluid.

A sketch of the computational domain and the definition of the coordinate system are given in Fig. 1(a), where R_c and R_i denote the circum-circle and in-circle radius, respectively. Details of the numerical setup and validations against experimental results can be found in Masoudi *et al.* [5]. Only key information is repeated here. Polygonal cylinders are placed at the centre of a cylindrical domain of $40D_i$ in diameter and πD_c in length (which is also the cylinder spanwise length), where D_c is the circum-circle diameter. Right-handed Cartesian coordinate systems are adopted at the centre of the domain, where the x'-y' system is fixed and equally splits the outer boundary into inlet and outlet surfaces, while the x-y system is set to align with the desired incident flow U_∞ direction; x, y and z are the streamwise, transverse and spanwise direction, respectively. The corresponding velocity components are u, v and w. Cylinders are fixed in the domain, while α is varied by changing the relative incoming flow direction.

Structured mesh with the number of cells in the radial (N_r) and circumferential (N_θ) directions are typically $216 \leq N_r = N_\theta \leq 224$, and $N_z = 56$ cells in the spanwise direction, where N_θ and N_r vary based on the specific polygon, aiming to ensure an equal distribution of cell divisions on each edge of a given polygon. The grid size grows exponentially in the radial direction (r) from the cylinder surface and is uniformly spaced in the circumferential direction (θ) and the spanwise direction (z). The cell growth rate in the r direction is set such that the maximum non-dimensional wall distance y^+ value is below unity. An example of the global mesh used to perform the computation is given in Fig. 1(b). Validation study [5] involved assessing time-mean C_D and St against the experimental data reported in Xu *et al.* [3] measured at the same Re, showing good agreement. Besides, the grid sensitivity examination indicates that the present mesh configuration and numerical scheme are capable of capturing more than 90% of turbulent kinetic energy, except near separation region, which is about 80%. Therefore, the current LES can be considered well-resolved for reliable subsequent analyses.

The governing Navier-Stokes equations and continuity equation for the current LES simulation are written as

$$\frac{\partial \bar{u}_i}{\partial x_i} = 0, \tag{1}$$

$$\frac{\partial \bar{u}_i}{\partial t} + \frac{\partial \bar{u}_i \bar{u}_j}{\partial x_j} = -\frac{1}{\rho}\frac{\partial \bar{p}}{\partial x_i} + \frac{\partial}{\partial x_j}\left[\nu\left(\frac{\partial \bar{u}_i}{\partial x_j} + \frac{\partial \bar{u}_j}{\partial x_i}\right) + \tau_{ij}\right], \tag{2}$$

where all the velocity and pressure components in the above equations are filtered quantities. The residual stress term τ_{ij} can be decomposed as

$$\tau_{ij} = \overline{u_i u_j} - \bar{u}_i \bar{u}_j. \tag{3}$$

Based on the eddy-viscosity type subgrid scale model, the sub-grid scale stress tensor τ_{ij} is modelled as

$$\tau_{ij} - \frac{2}{3}k_t \delta_{ij} = -2\nu_t\left(\bar{S}_{ij} - \frac{1}{3}\bar{S}_{kk}\delta_{ij}\right), \tag{4}$$

$$\bar{S}_{ij} = \frac{1}{2}\left(\frac{\partial \bar{u}_i}{\partial x_j} + \frac{\partial \bar{u}_j}{\partial x_i}\right), \tag{5}$$

where $\bar{S}_{ij}$ is the rate of the strain tensor in resolved scales; ν_t and k_t are subgrid scaled viscosity and turbulent kinetic energy, respectively. In this study, a typical value of Smagorinsky coefficient $C_s = 0.1$ is applied based on the successful validation of the circular cylinder flow [19, 20], and a wall-damping formulation proposed by Van Driest [21] is implemented as

$$\Delta = \min\left(\frac{k_v}{C_\Delta}, \Delta\right) \mathrm{y}\left[1 - \exp\left(\frac{-\mathrm{y}^+}{25}\right)\right], \tag{6}$$

where $k_v = 0.4187$ is the von Kármán constant and model constant $C_\Delta = 0.158$. No wall function is used in this study.

2.2. *Snapshot based POD*

POD analysis is performed on a subset of the LES data to examine the phase information of the vortex shedding behind all the tested cylinders. The selected two-dimensional (2D) subset spans a rectangular region of $-1D_i \leq x \leq 7D_i$ and $-1.5D_i \leq y \leq 1.5D_i$ at the mid-span ($z = 0$). It was found that the spanwise variation of the flow physics of interest is unimportant compared to that in the x-y plane [5, 16], and therefore only this 2D area is analysed. We made use of snapshots covering a duration of approximately 30 vortex shedding cycles after the transient period, at a time interval of $\Delta t^* = \Delta t U_\infty / D_i = 1$. This results in about 27 snapshots per shedding cycle. Fig. 2 presents example snapshots used for the present study, where the spanwise vorticity component $\omega_z = \partial v/\partial x - \partial u/\partial y$. The x and y coordinates are normalised by the constant cylinder in-circle diameter D_i, as x^* and y^*, respectively.

POD decomposes an ensemble of flow field data into an optimal combination of orthogonal basis functions and modes [22]. It has been successfully applied to reconstruct low-order dynamic models to extract large-scale coherent flow structures in turbulent wake flow behind bluff bodies and turbulent planar jet [23, 24, 25, among many others]. It has also been used to perform phase averaging and to evaluate the mean fluctuating motions and turbulence properties [26, 8]. Here, the snapshot based POD [27] is applied because of higher spatial dimension than temporal dimension.

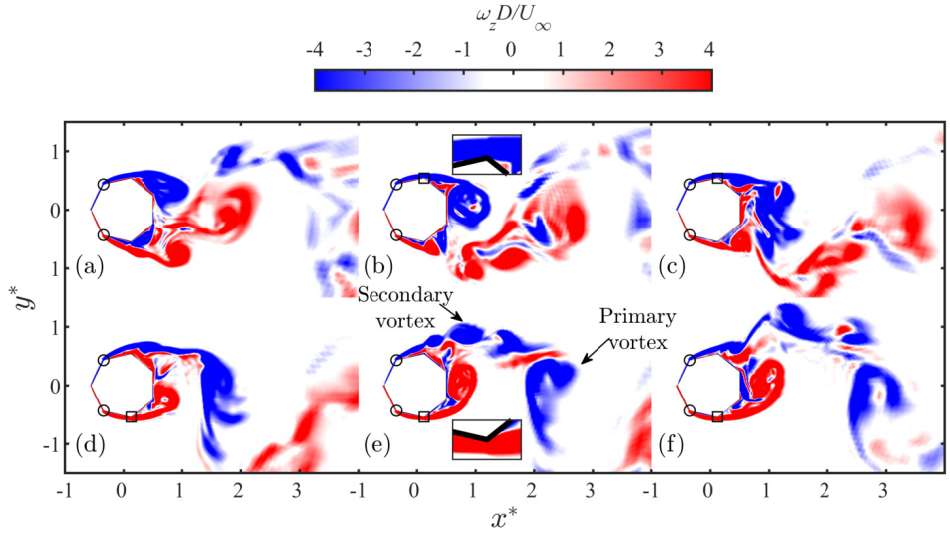

Figure 2: Instantaneous vorticity fields of $N = 7$, $\alpha^* = 0$ (corner orientation). (a–f) present example snapshots over $2/3$ of a vortex shedding cycle after the wake is fully developed, i.e., $2\pi/5$–$12\pi/7$. The local region of the temporary secondary separation points is magnified in (b) and (e). The arrows in (e) indicate the primary and the secondary vortices, with the secondary vortex emerging from the strongly flapping shear layer motion, which influences the appearance of the (temporary) secondary separation points. The primary separation points are marked by ○ and the secondary separation points by □.

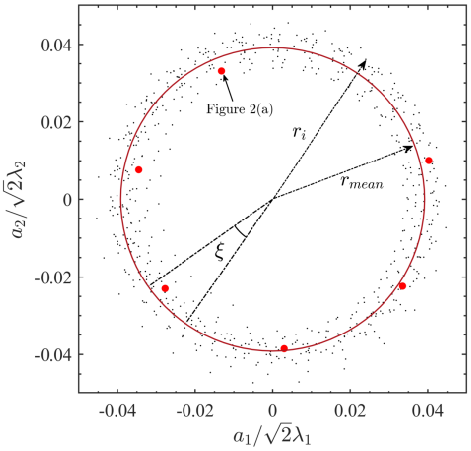

Figure 3: Scatter plot of modal coefficients associated with the highest modal energy a_1 versus a_2 for all the snapshots of case $N = 7, \alpha^* = 0$. r_i represents the radius of the i^{th} snapshot point, r_{mean} the mean radius marked by the red circle, and ξ marks the bin size for phase-averaging. The modal coefficients corresponding to the instantaneous flow fields presented in Fig. 2 are marked by the 6 red dots, where the one corresponds to Fig. 2(a) is labeled, and the remaining 5 are for Figs. 2(b)–2(e) in counterclockwise order.

Mathematically, the POD decomposition procedure can be summarised as follows, using velocity quantity as example

$$q'(\mathbf{x},t) = q(\mathbf{x},t) - \overline{q}(\mathbf{x}) = \sum_{n=1}^{N_t} a_n(t)\phi_n(\mathbf{x}), \tag{7}$$

where q' is the velocity fluctuation and $\overline{q}$ is the time-mean velocity, both are functions of space $\mathbf{x}$; N_t is the total number of snapshots used for decomposition. a_n and ϕ_n are the n^{th} POD coefficient and POD mode, respectively, which can be obtained by constructing the covariance matrix R.

$$R = U^T W U, \tag{8}$$

where $U = [\mathbf{u_1} \cdots \mathbf{u_n} \cdots \mathbf{u_{N_t}}]$, and $\mathbf{u_n}$ represents the two in-plane fluctuating velocity components (u,v) of the n^{th} snapshot available from LES, restructured into one column. The intensity of the spanwise velocity w is much lower and it does not have noticeable impact on the results. Here a spatial weighting matrix W is necessary to normalise the inner product because the LES data is stored in cylindrical coordinate structure. A standard eigenvalue problem is solved

$$R\psi_n = \lambda_n \psi_n, \tag{9}$$

where $n = 1 \cdots N_t$, and the eigenvalue λ_n denotes the energy content of the corresponding eigenvector ψ_n. By sorting λ_n in descending order, one may obtain a rank of the energy of the associated POD mode. The first few high-energy modes usually represent coherent flow structures or motion, while the higher-ranked low-energy modes often contain incoherent flow information or noise.

With the eigenvalues and eigenvectors determined from equation (9), the n^{th} POD mode ϕ_n in equation (8) can be calculated by

$$\phi_n = \sqrt{W} U \psi_n \frac{1}{\sqrt{\lambda_n}}. \tag{10}$$

The W term on the *rhs* accounts for the non-uniform mesh grid weighting. Accordingly, the POD coefficient a_n is calculated as

$$a_n = U^T \sqrt{W} \psi_n. \tag{11}$$

2.3. POD-based phase averaging

The first two modal coefficients associated with the highest energy can be used to extract the phase information of the periodic vortex shedding as demonstrated by Oudheusden *et al.* [8], and are less affected by phase jitter [28] which generally occurs while estimating the phase by performing local or truncated field information like pressure signals. The phase angle φ_i for the i^{th} snapshot is related to the first two modal coefficients a_1 and a_2 by

$$a_1 = r_i \sqrt{2\lambda_1} \sin(\varphi_i), \quad a_2 = r_i \sqrt{2\lambda_2} \cos(\varphi_i). \tag{12}$$

It is not difficult to see that

$$\frac{{a_1}^2}{2\lambda_1} + \frac{{a_2}^2}{2\lambda_2} = r_i^2, \tag{13}$$

where r_i is the radius of the coefficient space for the i^{th} snapshot.

Figure. 3 shows the scatter plot of the first two POD mode coefficients, a_1 and a_2. Every dot represents one instantaneous flow field snapshot. The distribution of a_1 and a_2 around the circle of the mean radius r_{mean} is evident and the scattering of the dots around r_{mean} is attributed to the coherency fluctuation of the vortex shedding pattern. That is, those having smaller radii usually show clear vortex structures, while for those having larger radii, vortices tend to be distorted and fragmented. A bin size of $\xi = \varphi \pm \pi/18$ is chosen to perform the phase averaging in this study. Typically each bin contains about 35 snapshots. The chosen bin size is a result of considering the balance between the convergence of phase averaging and the desired phase resolution to resolve vortex strength and its position (or phase) as correctly as possible. A convergence test related to the bin size was performed (figure not shown) to evaluate the effect of the bin size on the outcomes. The results indicate that reasonable bin size variation does not have a strong effect on the phase averaged results for this level of bin filling, aligning with the findings of Oudheusden *et al.* [8]. This reassures adequate statistical convergence for the order of the quantities studied here.

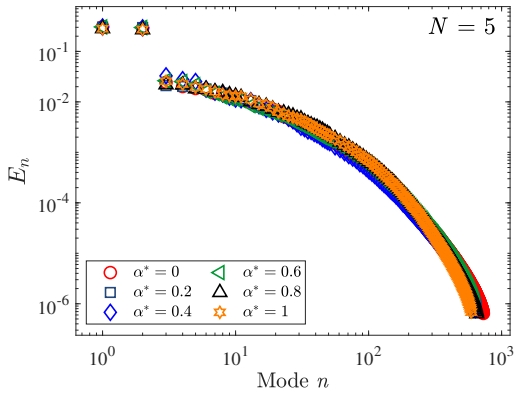

Figure 4: POD mode energy distribution of the pentagon cylinder at various α^*. $N = 5$ is used as an example.

It is worth clarifying that phase averaging of the present data may equivalently be performed based on the time-resolved lift coefficient $C_L(t)$, which is available from the LES simulation. The POD-based phase averaging directly makes use of the flow field information only, whose synchronisation to the aerodynamic forces on the bluff-body may not always be guaranteed. It can also be applied to data obtained from a non-time-resolved PIV experiment without force measurement [15]. More importantly, POD offers some preliminary analysis based on the spatial distribution of its orthogonal modes, which is relevant to the statistical analysis discussed later in Section 3.2.

3. Results and discussion

3.1. POD analysis of the wake flow

Figure. 4 shows the distribution of the modal energy E_n of the six α^* cases for the pentagon, in descending order, where $E_n = \lambda_n / \sum_{n=1}^{N_t} \lambda_n$. E_n represents the relative contribution of the corresponding eigenmode to the total fluctuation kinetic energy, and as expected, the first two modes share similar energy level, each taking about 27% of the total energy. The higher modes have much lower energy level and decrease rapidly. This pattern resembles the classical Kármán vortex shedding. α takes negligible effect on the energy content of the first two modes, and only subtly influences the energy contribution of the higher modes, representing less coherent vortex structures or turbulence. Other polygons display similar patterns, i.e., distinctively high and similar energy content of the first two modes, and insignificant α effect.

The spatial distribution of the first two POD modes ϕ_1 and ϕ_2, on the basis of $u'v'$, are shown in Fig. 5 for eight selected cases. The two modes reflect anti-symmetric structures with a pattern shift of about $1/4$ of a wavelength in the streamwise direction, which is associated with a $1/4$ period offset between $a_1(t)$ and $a_2(t)$ (figure not shown). It resembles the downstream convection of the vortex street [29, 30]. The asymmetric distribution of the mode structure for cylinders at off-principal orientations is also clearly seen in Fig. 5.

The selected cases shown in columns 3 and 4 of each row in Fig. 5 correspond to the α^* cases showing the furthest shear layer penetration distance into the wake behind the cylinders of the same N. These cases also have the smallest C_D and largest St, as well as the most stable shear layer dynamics reflected as the weakest flapping motion strength and the thinnest shear layer in the time-mean sense [16]. These features can be seen, although subtly, by comparing columns 1 and 3 for the same row, i.e., a smaller growth rate of the mode packet size in the streamwise direction and a smaller wavelength (streamwise distance between the neighbouring packets of the same sign) corresponding to higher St.

3.2. Asymmetric evolution of coherent vortcies in the wake

Since instantaneous flow fields are typically turbulent (Fig. 2), we follow a method similar to that introduced in Wang *et al.* [15] to identify coherent vortex packets in the wake. The procedure is summarised in Fig. 6.

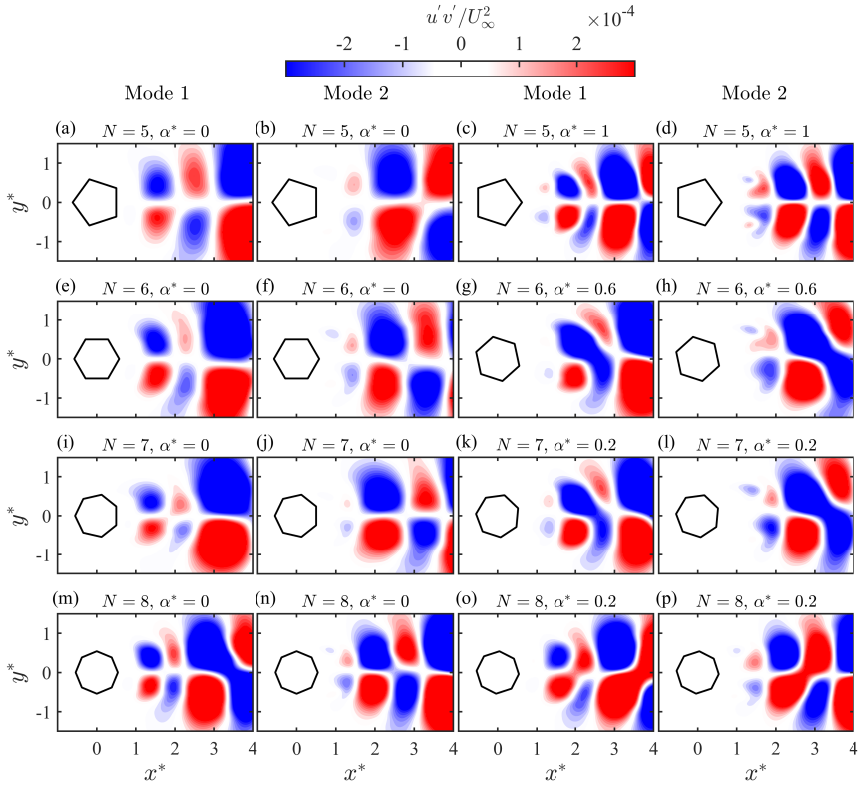

Figure 5: POD mode 1 (the first and third columns) and mode 2 (the second and fourth columns) of selected cases. The contours are based on $u'v'$.

We first apply POD-based phase-averaging process to instantaneous flow fields (Fig. 6 a) following the procedure explained in Section 2.2 and 2.3. The phase-averaged vorticity field $\langle \omega_z \rangle$ is shown in Fig. 6(b), where coherent vortices are more easily identifiable. A common vortex identification method Q-criterion proposed by Hunt *et al.* [31], Fig. 6(c), is then applied to quantify the circulation and motion trajectories of these vortices. In the case of the 2D flows, Q can be calculated as

$$\begin{aligned} Q &= \frac{1}{2}\left(\|\Omega_{ij}\|^2 - \|S_{ij}\|^2\right) \\ &= -\frac{1}{2}\left[\left(\frac{\partial u}{\partial x}\right)^2 + \left(\frac{\partial v}{\partial y}\right)^2\right] - \frac{\partial u}{\partial y}\frac{\partial v}{\partial x}, \end{aligned} \tag{14}$$

where Ω_{ij} and S_{ij} are the rotational and strain rate tensors, respectively; Q is the positive second invariant of the velocity gradient tensor, which can be considered as the region where rotation exceeds strain. An appropriately selected low-level universal threshold $Q(D_i/U_\infty)^2 = 0.2$ is set to individualise the vortex packets after numerous sensitivity tests. An in-house developed iterative segmentation algorithm is then applied to the Q field in (c) to define the vortex boundaries. The centroid coordinates of each vortex packet (x_c, y_c) is calculated as the $\langle \omega_z \rangle$ weighted-centroid [29]

$$\begin{aligned} x_c &= \frac{1}{\Gamma}\oint_A x\langle \omega_z \rangle \, \mathrm{d}A, \\ y_c &= \frac{1}{\Gamma}\oint_A y\langle \omega_z \rangle \, \mathrm{d}A, \end{aligned} \tag{15}$$

where Γ is the circulation of each vortex packet,

$$\Gamma = \oint_A \langle \omega_z \rangle \, \mathrm{d}A, \tag{16}$$

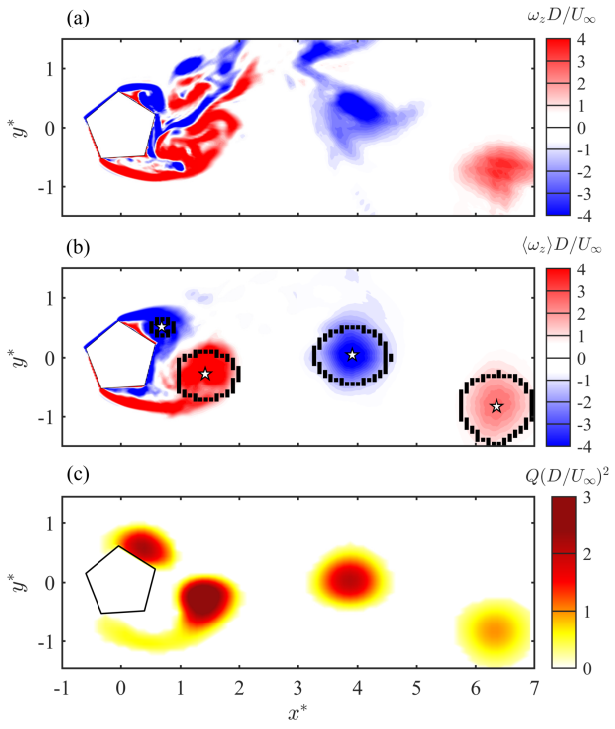

Figure 6: Procedure for coherent vortex identification, using case $N = 5, \alpha^* = 0.4$ as an example. (a) Instantaneous ω_z field; (b) the corresponding phase-averaged vorticity $\langle\omega_z\rangle$ field, with the vortex packet centroids marked by ☆, the identified boundaries of the vortices are marked in black; (c) the corresponding Q contour.

and A is the internal area enclosed by the boundaries shown in Fig. 6(b), where the calculated vortex centroids are also marked.

The phase-averaged vorticity fields, which match the phases shown in Figs. 2(c)–2(f), are presented in Figs. 7(a)–7(d). While all the other cases investigated in this study display the classical Kármán vortex shedding with a single distinctive peak at the Strauhal frequency in the $v'(t)$ frequency spectrum, only case $N = 7, \alpha^* = 0$ shows a second peak at a higher frequency; see Fig. 7(e), where the same spectrum for case $N = 7, \alpha^* = 1$ is also included for comparison. Here, the Strouhal number is defined as $\mathrm{St} = fD_i/U_\infty$, where f is the frequency of the $v'(t)$ signal. The sampling point in each case is located at the centroid of the newly rolled-up primary vortex just ready to be convected downstream, identified in the phase-averaged fields. Note the similar Strauhal frequency (the first peak) of the two cases shown here [5].

The spectrum peak at 2St for case $N = 7, \alpha^* = 0$ is not a simple superharmonic, but indicates the physical shedding of secondary coherent vortices, labeled in Fig. 7(c). Secondary vortices are not easily distinguishable from the Kelvin-Helmholtz like vortices in the instantaneous vorticity field of the shear layer shown in Fig. 2(e), but are better manifested in the phase-averaged fields. They are not to be considered as 'strong' Kelvin-Helmholtz like vortices, since the latter do not leave clear footprints in the v' spectrum; see the 7F spectrum in Fig. 7(e). Note that this second peak was also noticed in the fluctuating wall shear stress spectrum of this particular case between the secondary separation point (see Fig. 2 for their locations) and the immediate corner downstream (in the base area) [16], which is owing to the secondary vortex shedding too. It however is not reported in Wang *et al.* [15], plausibly due to the lower spatial resolution of their PIV experiment.

The secondary vortex shedding is only observed in case $N = 7, \alpha^* = 0$, among all the 24 testing cases. The exact physical origin of this unique observation, which is probably related to the special local geometry near the primary separation points (see Fig. 2 for their locations), is left for a future study. Even though the two peaks in Fig. 7(e) are of similar magnitude, suggesting similar strength of the primary and the secondary vortices at the sampling point

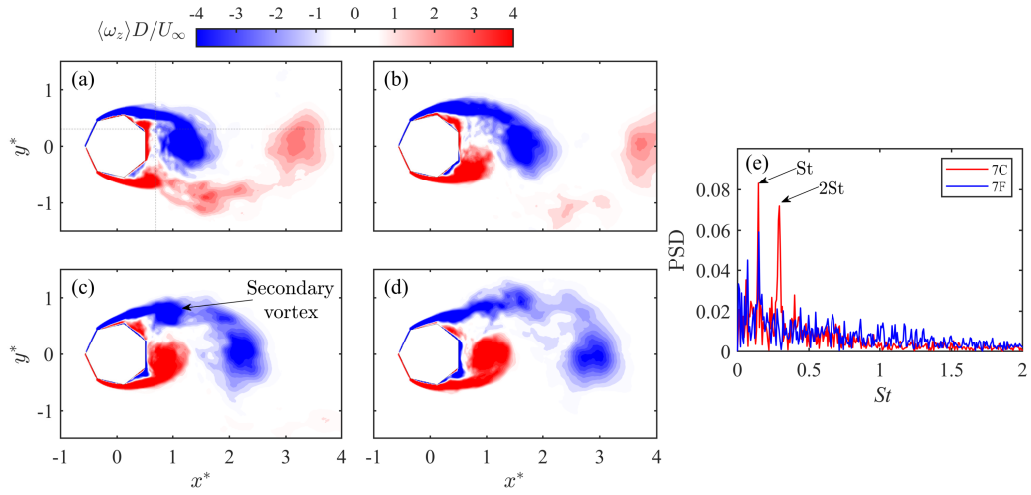

Figure 7: (a)–(d): Phase-averaged vorticity fields corresponding to the instantaneous fields shown in Figs. 2(c)–2(f). (e) PSD (in arbitrary unit) of $v'(t)$, sampled at the point shown in (a); 7C stands for the case $N = 7, \alpha^* = 0$. For comparison, $v'(t)$ spectrum was plotted for $N = 7, \alpha^* = 1$, marked as 7F, sampled at a similar location.

location, secondary vortices are less coherent and shorter lived. For instance, the motion of the secondary vortices in the transverse direction is appreciably different to that of the primary ones, as can be inspected in Fig. 7(c) and 7(d). As the primary vortex moves inwards across the wake centerline to the other side of the wake region, the secondary vortex advects outwards in the opposite transverse direction, mostly due to the resultant induced velocity from the two (upper and lower side) primary vortices. Also attributing to the influence of the two primary vortices, the coherence of the secondary vortex is quickly lost; see Fig. 7(d).

Cases of $0 < \alpha^* < 1$ all result in asymmetric wake behind them, which have been addressed in terms of the time-mean near wake flows [5]. This asymmetry mean flow must originate from the asymmetric circulation of the coherent vortices shed from the top and the bottom side, and their asymmetric evolution trajectories, which are discussed next.

3.2.1. Vortex trajectory

The trajectories of the coherent vortex centroid (x_c, y_c) as calculated by equation 15 are shown in Fig. 8 for all the testing cases, including that for the secondary vortices in case $N = 7, \alpha^* = 0$. For cylinders at their principal orientations, the vortex trajectories basically resemble the findings in experiment [15]. For off-principal orientations, asymmetric trajectories about $y = 0$ between the upper and lower vortices may be noticed, especially at large x^*, where off-set (deviation from symmetry) is more obvious (see the red-highlighted case in each sub-figure for example). Closer inspection reveals that off-set direction varies, even though α^* universally increments in the same clock-wise direction for all the cases. For $N = 5$, off-sets are all negative ($y < 0$), whilst for $N = 6, 7$ they are positive ($y > 0$). The off-sets for $N = 8$ cylinders are very small and subtle, in the sense that those for $\alpha^* = 0.2, 0.4$ are negative and $\alpha^* = 0.6, 0.8$ are positive. These are in line with the trend of the time-mean C_L sign and the time-mean wake off-set quantified previously [5].

The special case $N = 7, \alpha^* = 0$, where secondary vortices emerge in the separated shear layer, is also highlighted in Fig. 8(c). The opposite convection directions of primary and secondary vortices discussed qualitatively above are confirmed. Because of their mutual interaction, secondary vortices also significantly influence the trajectories of primary vortices, resulting in their unique behaviour. In particular, the primary vortex trajectories cross the centreline $y = 0$, i.e., centroids of the positive and negative sensed primary vortices switch side at $x^* \approx 2.7$, and then remain close to $y = 0$, while those for all the other cases always move further apart in the transverse direction.

A common feature of the near field development of all the trajectories shown in Fig. 8 is that primary vortices firstly move towards $y^* = 0$ until $x^* \approx 1.2$–1.5. We may use this feature to define the vortex formation distance L_c, as shown in Fig. 9, which is equivalent to the formation length L_f commonly defined based on the peak root-mean-squared (rms) u' along $y = 0$ [15]. L_c is instead defined by the x-coordinate of the primary vortex trajectory *turning point*, i.e.,

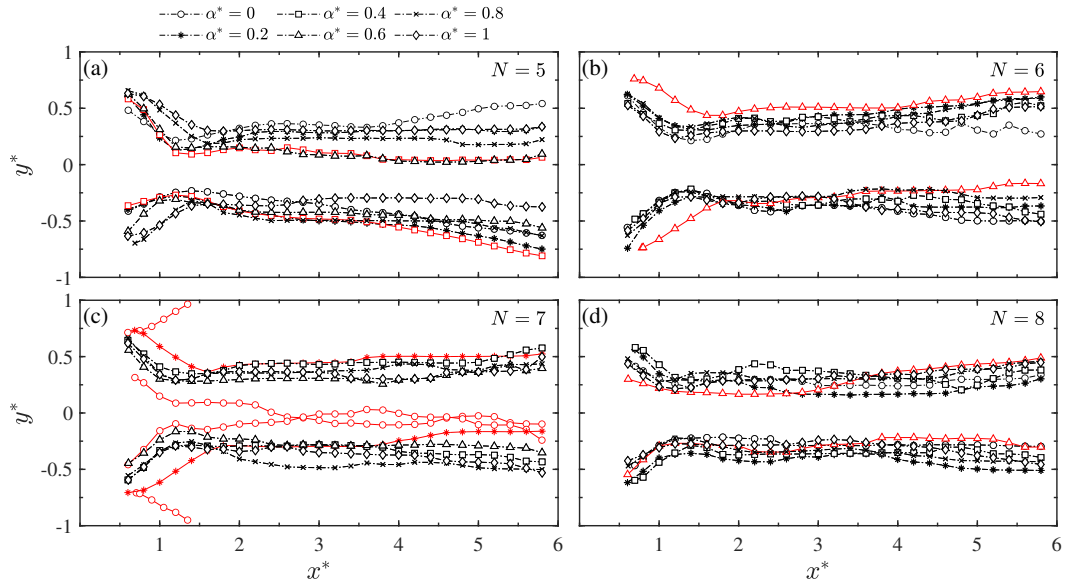

Figure 8: Primary vortex centroid trajectories, including the secondary vortex centroid trajectories in $N = 7, \alpha^* = 0$ (c). The most asymmetric cases of each N, as well as case $N = 7, \alpha^* = 0$, are highlighted in red solid line.

the smallest x_c where $\mathrm{d}y_c/\mathrm{d}x_c \approx 0$ (for most cases) or where the value of $\mathrm{d}y_c/\mathrm{d}x_c$ changes appreciably (for the few cases displaying strong wake asymmetry). The location of this turning point is also assured by manual inspection. Accordingly, the transverse distance between the upper and lower L_c points, denoted as L_c^U and L_c^L, respectively, is defined as D_c.

In this work, L_c is used to quantify the vortex formation distance instead of L_f because of two reasons. First, formation distances for upper and lower primary vortices differ at off-principal orientations, while L_f is a unique quantity for a given polygon in a given flow condition. Second, determination of L_f relies on good data statistical convergence, which is not sufficiently achieved in this study due to relatively small simulation duration (30 cycles).

Masoudi *et al.* [16] demonstrated that the time-mean shear layer penetration distance in the streamwise direction, $x_\delta^{T,B}$, for the upper and lower side, respectively, is a suitable characteristic length scale. L_f, on the other hand, is a widely accepted universal characteristic length scale for bluff bodies, supported by numerous studies, e.g., Wang *et al.* [4] for polygonal cylinders at $\alpha^* = 0, 1$. The physical equivalence of L_c and L_f therefore suggests that the former should be correlated with x_δ, and this is shown in Fig. 10(a).

The associated transverse distance D_c is found to be correlated with the back pressure coefficient C_{pb} (as indicated in Fig. 10(b)), averaged in both time and spatial sense, where $C_{pb} = 2\left(p_b - p_\infty\right) / \left(\rho U_\infty^2\right)$ with p_b and p_∞ being the base and free stream static pressure, respectively. The spatial average is performed over the base area between the upper and lower primary separation points, where the pressure variation is appreciably small compared to that over the windward area [5]. The correlation, which is positive, makes sense since stronger (larger Γ magnitude) coherent vortices rolled up behind the base area induce larger velocity, which in turn reduces the pressure over the base area. On the other hand, stronger vortices tend to be large in size and associated with a small D_c value. Case $N = 7, \alpha^* = 0$ has a particularly small value of D_c, in line with Fig. 8(c), and is further away from the correlation line compared to the other cases. This is due to the influence of the secondary vortices. Also as expected, D_c correlates well with the characteristic wake width extracted from the time-mean velocity field (figure not shown).

3.2.2. Vortex circulation

Wang *et al.* [15] showed that circulation Γ of coherent vortices behind polygonal cylinders at $\alpha^* = 0$ and 1, calculated by equation 16, maximises at $x \approx L_f$. The maximum Γ value, denoted as Γ_{max}, scales with the characteristic wake width, which further scales with the drag coefficient C_D. In this section, drag and lift coefficients are calculated

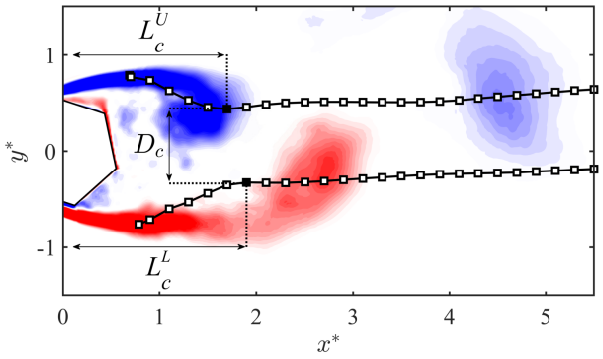

Figure 9: Definition of characteristic length scales L_c and D_c, using case $N = 6, \alpha^* = 0.6$ as example. The background contour is $\langle \omega_c \rangle$ field at an arbitrary phase. Vortex trjectories going through the vortex centroids is reassured.

as

$$C_D = \frac{F_x}{\frac{1}{2}\rho U_\infty^2 (L_z D_i)}, \quad C_L = \frac{F_y}{\frac{1}{2}\rho U_\infty^2 (L_z D_i)}, \tag{17}$$

where F_x and F_y are the total force in the x and y direction, respectively, and L_z is the cylinder length. They are both time-mean values by default; the instantaneous lift coefficient is denoted as $C_L(t)$. For $0 < \alpha^* < 1$, Γ_{max} magnitude for the upper and lower side differ, and the x-coordinate where Γ_{max} occurs for each side is also asymmetric, but consistently close to L_c. Fig. 11(a) presents Γ_{max} in its dimensionless form, defined as $\Gamma^*_{max} = |\Gamma_{max}|/(U_\infty D_i)$. Hereafter the asterisk on Γ is omitted for clarification purpose. For case $N = 7, \alpha^* = 0$, only Γ_{max} for primary vortices are shown. By the time primary vortices maximise (at $x \approx L_c$), secondary vortices are not yet formed (see Fig. 7a).

Figure 11(a) confirms that the magnitude of Γ^L_{max} (> 0) and Γ^U_{max} (< 0) may differ significantly for some off-principal orientations. For instance, variation dependence of $|\Gamma^U_{max}|$ on α^* is appreciably different to that of $|\Gamma^L_{max}|$ for $N = 6$, and the two values at $\alpha^* = 0.2$ and 0.4 differ obviously, as well as $N = 5, \alpha^* = 0.6$. At principal orientations, $|\Gamma^U_{max}|$ and $|\Gamma^L_{max}|$ are very close and the average values are shown. Their variation trends are also approximately consistent with the experimental study [15]. Note that in the experimental study, the length scale used for non-dimensionalisation is the cylinder projection width, which varies with N and α^*, whilst here the universal D_i is used, which provides a direct comparison of $|\Gamma_{max}|$. It is worth noting that the difference of the vortex strength between the upper side and the lower side in the principal orientation is considerably small, $\overline{|\Delta\Gamma^{U,P}_{\max}|} = 0.03$, which is anticipated given the symmetric orientation to the incident flow direction. It lends additional credibility to the current findings.

According to Birkhoff and Zarantonello [32], and Berger [33], the raw vortex circulation $|\Gamma_{max}|$ is associated with U_∞ via a dimensionless quantity $\mathscr{E}$ as

$$\mathscr{E} = \frac{|\Gamma_{max}| f_{vs}}{U_\infty^2}, \tag{18}$$

where f_{vs} is the Strouhal frequency. For a circular cylinder, Schaefer and Eskinazi [34] obtained a value of $\mathscr{E} = 0.343$ from an analytic model of vortex street generated in a viscous flow at $\mathrm{Re} = 62$. Experimentally, Koopmann [35] found $\mathscr{E} = 0.32$ for a vibrating cylinder for Re=200 and Berger [36] obtained a value of $\mathscr{E} = 0.39$ at $\mathrm{Re} = 65$ and 151. In the present study, $0.39 < \mathscr{E} < 0.53$ for both upper and lower side, mostly around 0.45, which is in good agreement with the theoretical value of 0.5[32] derived from the laminar parabolic boundary layer theory.

Griffin *et al.* [37, 38] found that the circulation (Γ_{max}) of the vortices in the wake behind a circular cylinder vibrating in transverse direction (lateral vibration) is approximately inversely correlated with the ratio of vortex formation length (L_f) to the wake width (D_w). The stationary cylinder can be considered as being vibrating at an infinitesimal amplitude and hence this correlation plausibly holds. This is shown in Fig. 11(b). Here, in order to account for the

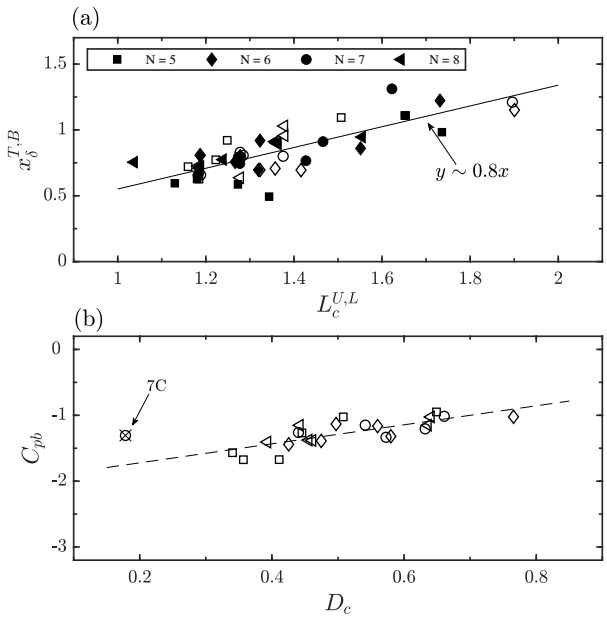

Figure 10: (a) Correlation between $x_\delta^{T,B}$ and $L_c^{U,L}$; the solid markers are for the upper side and the open markers are for the lower side; (b) Dependence of the base pressure coefficient C_{pb} on D_c; legends follow (a). Correlation excludes case $N = 7, \alpha^* = 0$ (labelled as 7C).

asymmetric Γ_{max} and L_f at off-principal orientations, we replace L_f with $L_c^{U,L}$ obtained from §3.2.1. The empirical fitting function can be written as

$$\frac{L_c^{U,L}}{D_w} = -0.45\left|\Gamma_{max}^{U,L}\right| + 2.65. \tag{19}$$

The R^2 value for this fitting function stands at 0.71, indicating a robust representation of the dataset, especially when accounting for the inherent variability and turbulent characteristics of the flow. This is consistent with the positive correlation of C_D and Γ_{max} which will be discussed later, since D_w is positively correlated with C_D[4, 15].

Masoudi *et al.* [16] noticed that instantaneous shear layers flap in the transverse direction. The strength of this flapping motion correlates with x_δ, and impacts C_D and St. The phase information resolved in the present study facilitates direct quantification of the flapping motion amplitude in the time domain instead of in the frequency domain as in Masoudi *et al.* We thus examine the transverse position of the separated shear layer centre, where $|\omega_z|$ maximizes, for every resolved phase at a constant location of $x^* = 0.4$. This streamwise sampling location is chosen to minimise the influence of the rolled up vortices. The true flapping amplitude, normalised by D_i and denoted as Φ, is further estimated by a sinusoidal function fit in order to account for the limited phase resolution (figure not shown). Fig. 11(b) demonstrates a reasonable positive correlation between Φ and $|\Gamma_{max}|$, with the upper and lower shear layer separated. It suggests that stronger shear layer flapping motion results in vortices of larger circulation in general. Case 7C has a slightly higher value of Φ, which plausibly suggests that the stronger flapping amplitude is attributed to the secondary vortices; see Fig. 7.

Kutta-Joukowski theorem states that $C_L(t) \propto -\Gamma_p(t)$, the circulation around the polygonal cylinder surface. According to Kelvin's circulation theorem, $-\Gamma_p(t) = \Gamma_s(t) + \Gamma_v(t)$, where Γ_s and Γ_v are the instantaneous circulation associated with the separated shear layer and the rolled up vortices, respectively. Masoudi *et al.* [16] found that the difference between x_δ^T and x_δ^B, extracted from the time-mean vorticity field where periodically rolled up vortices manifest totally as shear-like structure, is linearly correlated with C_L, including the sign effect. When $\alpha^* = 0$ and 1, two shear layers are of the same length, and therefore $C_L = 0$. Consider the phase (or the instant time t) where Γ_{max} occurs for either the upper or the lower side, if the magnitude $|\Gamma_s| \ll |\Gamma_v|$, then $\Gamma_{max} \sim C_L(t, \max/\min)$. This further suggests that the difference of the vortex strength

$$\left|\Gamma_{max}^L\right| - \left|\Gamma_{max}^U\right| \sim C_L(t, \max) + C_L(t, \min), \tag{20}$$

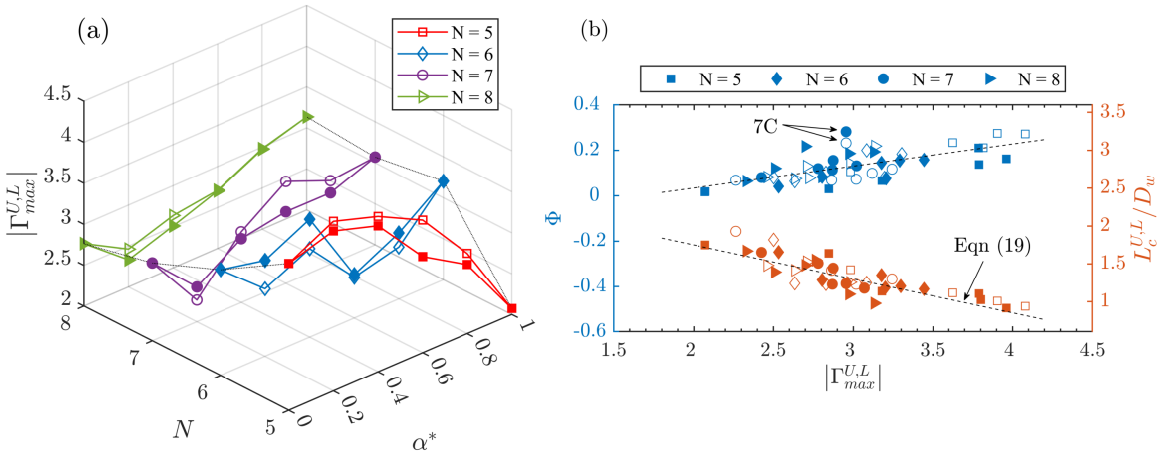

Figure 11: (a) Dependence of the maximum circulation Γ^*_{max} on N and α^*; (b) Dependence of the shear layer flapping motion strength Φ and the ratio $L_c^{U,L}/D_w$ of the vortex formation distance and the wake width on Γ^*_{max}. The solid and open markers are for the upper and lower side, respectively, denoted as $|\Gamma^U_{max}|$ and $|\Gamma^L_{max}|$.

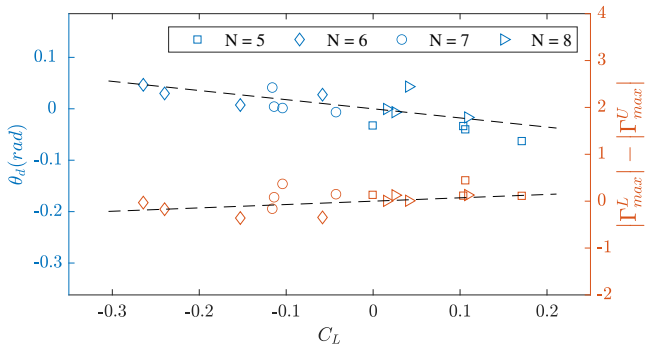

Figure 12: Dependence of the trajectory deflection angle θ_d and $|\Gamma^L_{max}| - |\Gamma^U_{max}|$ on C_L. Cases of $\alpha^* = 0, 1$ are excluded because their C_L, θ_d and $|\Gamma_{max}|$ difference are all zero.

which further scales with the time-mean C_L. Note that $C_L(t, \max) > 0$ and $C_L(t, \min) < 0$ always. This correlation is shown in Fig. 12, where the non-zero Γ_s is responsible for the weak correlation.

Figure 12 also shows that C_L reasonably correlates with the wake deflection angle θ_d derived from the trajectories of primary vortices. The negative correlation can be understood from the momentum balance in the transverse direction on a control volume enclosing the cylinder. Here $\theta_d = \mathrm{d}\left(y_c^U + y_c^L\right)/\mathrm{d}x_c$ averaged over $x_c > L_c$, where y_c^U and y_c^L are the y-coordinate of the upper and lower vortex trajectory, respectively, at a given x_c. Evidenced in Fig. 8, trajectories for $x_c > L_c$ are fairly straight for most cases, which lends support to the validity of quantifying θ_d based on the averaged slope. Closer examination of the marker distribution indicates that as N increases, θ_d tends to cluster more closely around 0, which suggests that the trajectories tend to be more symmetric and less influenced by α. As can be expected, θ_d, as well as C_L, will eventually vanish for the circular cylinder $N = \infty$.

Having looked at Γ_{max} asymmetry, we examine the property of $\left|\Gamma^L_{max}\right| + \left|\Gamma^U_{max}\right|$. Perhaps as expected, this quantity is correlated with X_{peak}, the amplitude of the primary peak of the C'_L spectrum, defined as

$$X(f) = \int C'_L(t) \exp(-2\pi j f t) dt. \tag{21}$$

This is illustrated in Fig 13(a) which exhibits a fairly significant correlation. That is, the fluctuating lift coefficient directly indicates the strength of the shed vortices.

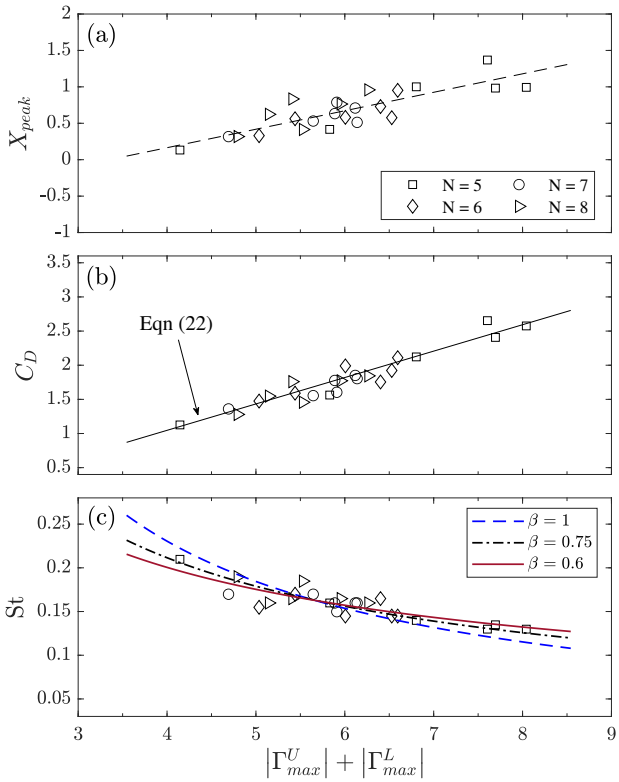

Figure 13: Correlation between $|\Gamma^U_{max}| + |\Gamma^L_{max}|$ and X_{peak} (a), and C_D (b), and St (c). Equation (22) is presented in (b). Fitting curves with various β values (Equation 27) are also shown in (c).

Hu *et al.* [9] calculated the circulation of vortices behind rounded corner square prisms and found that it is proportional to C_D. This is also supported by Wang *et al.* [15], as mentioned above. Larger circulation induces stronger velocity over the cylinder base area, reduces C_{pb} and increases C_D, which is consistent with the correlation shown in Fig. 10(b). Figure 13(b) demonstrates a fairly clear correlation between C_D and $|\Gamma^U_{max}| + |\Gamma^L_{max}|$, regardless of N and α^* in the tested range. The correlation can be described by a relatively simple function

$$C_D \approx 0.4\left(|\Gamma^U_{max}| + |\Gamma^L_{max}|\right) - 0.5. \tag{22}$$

Lamb-Oseen (LO) vortex model is often utilised to model coherent vortices behind circular and polygonal cylinders [3, 39, 40]. In this model, velocity components (u_r, u_θ, u_z) are given by

$$\begin{aligned} u_r = 0, \qquad u_z = 0, \\ u_\theta(r,t) = \frac{\Gamma}{2\pi r}\left[1 - \exp\left(-\frac{r^2}{4\nu t}\right)\right]. \end{aligned} \tag{23}$$

Here a local cylindrical coordinates centred at the vortex is adopted. Following the arguments in Xu *et al.* [3], energy balance implies that drag force F_D produced by a pair of vortices formed over one cycle period, which travels a distance of one wavelength λ, is related to the kinetic energy budget as $2KE = F_D\lambda$ [17], where KE is the kinetic

energy associated with an isolated LO vortex, viz.

$$\begin{aligned} KE &= \int_0^\infty \rho \pi r u_\theta^2 \mathrm{d}r \\ &= \rho \frac{\Gamma^2}{4\pi} \int_0^\infty \frac{1}{r} \left[1 - 2\exp\left(-\frac{r^2}{4\nu t} \right) + \exp\left(-\frac{2r^2}{4\nu t} \right) \right] \mathrm{d}r \\ &= \rho \frac{\Gamma^2}{4\pi} g(t). \end{aligned} \tag{24}$$

Thus, considering the energy balance over a shedding cycle, we have

$$C_D \left(U_\infty^2 D_i \right) \left(\frac{U_\infty}{f_{vs}} \right) \sim \Gamma^2 g(t), \tag{25}$$

and therefore

$$C_D \sim \left(\frac{\Gamma}{U_\infty D_i} \right)^2 g(t) \mathrm{St}, \tag{26}$$

where $U_\infty / f_{vs} \sim \lambda$. Since $C_D \sim \Gamma$ (equation 22), equation 26 suggests that $\mathrm{St} \sim \Gamma^{-1} \sim C_D^{-1}$. The first relation indicates that the shedding frequency of vortices is inversely proportional to their strength, and the second inverse relation between C_D and St has been confirmed by numerous studies. To be specific, we can write

$$\mathrm{St} \sim C_D^{-\beta} \sim \left(\left| \Gamma_{max}^U \right| + \left| \Gamma_{max}^L \right| \right)^{-\beta}, \tag{27}$$

with β values proposed in the literature, e.g., $\beta = 1$ [41], $\beta = 0.75$ [42] and $\beta = 0.6$ [3]. Comparison of the three β values are made in Fig. 13(c), where all three curves show reasonably good fitting quality for cylinders at all incidence angles, with $\beta = 0.6$ slightly better.

4. Conclusions

In this paper, the evolution of coherent vortices shed behind polygonal cylinders of side number $N = 5$–8 in incident flows of $\mathrm{Re} = 10^4$ is studied utilising LES data and POD-based phase averaging. Vortices separated from upper and lower shear layers are treated separately, in terms of their centroid trajectory and maximum circulation, Γ_{max}^U and Γ_{max}^L.

Vortex shedding behind all the tested cases are of classical Kármán type, with a distinctive peak at the Strauhal frequency in the transverse velocity frequency spectrum, except the heptagon at corner orientation, where a clear secondary vortex pair is shed accompanying every primary vortex pair. These secondary vortices are short lived and their trajectories are in the opposite direction to that of the primary vortices, which basically resemble those in all the other cases. A trajectory deflection angle θ_d is defined and is found to be correlated with C_L, which is clearly non-zero at off-principal orientations. POD energy distribution shows that all the cases have approximately the same energy content for the first two modes, each having about 30% of the total energy.

Based on the trajectory, vortex formation distance L_c is defined on each side of the wake, where Γ_{max}^L and Γ_{max}^U occur. The two circulation display appreciable asymmetry at off-principal orientations. Individually, $\Gamma_{max}^{U,L}$ magnitude correlates with shear layer flapping motion strength. It was also found that $\left| \Gamma_{max}^L \right| + \left| \Gamma_{max}^U \right|$ correlates with C_D positively and St inversely, while $\left| \Gamma_{max}^L \right| - \left| \Gamma_{max}^U \right|$ correlates positively, albeit weakly, with C_L. The associated characteristic wake width D_c is found to be positively correlated with the averaged based pressure coefficient C_{pb}.

Acknowledgements

This research was supported by the National Natural Science Foundation of China (Grant Nos. 12111530102 and 12272163), the Natural Science Foundation of Shenzhen Municipality (Grant No. 20220814230752003), Durham University Doctoral Scholarship (DDS) program and the Royal Society International Exchanges (Grant No. IEC/NSFC/201061). The authors are grateful to the support from the Center for Computational Science and Engineering at Southern University of Science and Technology, as well as the Advanced Research Computing Center of Durham University.

The authors report no conflict of interest.

Data availability

The data that support the findings in this manuscript can be obtained from the corresponding author upon reasonable request

References

[1] W.-L. Chen, Y. Huang, C. Chen, H. Yu, D. Gao, Review of active control of circular cylinder flow, Ocean Engineering 258 (2022) 111840.
[2] S. Rashidi, M. Hayatdavoodi, J. A. Esfahani, Vortex shedding suppression and wake control: A review, Ocean Engineering 126 (2016) 57–80.
[3] S. Xu, W. Zhang, L. Gan, M. Li, Y. Zhou, Experimental study of flow around polygonal cylinders, Journal of fluid mechanics 812 (2017) 251–278.
[4] Q.-Y. Wang, S.-J. Xu, L. Gan, W.-G. Zhang, Y. Zhou, Scaling of the time-mean characteristics in the polygonal cylinder near-wake, Experiments in Fluids 60 (12) (2019) 1–15.
[5] E. Masoudi, L. Gan, D. Sims-Williams, Large eddy simulation of incident flows around polygonal cylinders, Physics of Fluids 33 (10) (2021) 105112.
[6] N. Agrwal, S. Dutta, B. K. Gandhi, Experimental investigation of flow field behind triangular prisms at intermediate reynolds number with different apex angles, Experimental Thermal and Fluid Science 72 (2016) 97–111.
[7] D. A. Lyn, S. Einav, W. Rodi, J.-H. Park, A laser-doppler velocimetry study of ensemble-averaged characteristics of the turbulent near wake of a square cylinder, Journal of Fluid Mechanics 304 (1995) 285–319.
[8] B. Van Oudheusden, F. Scarano, N. Van Hinsberg, D. Watt, Phase-resolved characterization of vortex shedding in the near wake of a square-section cylinder at incidence, Experiments in Fluids 39 (1) (2005) 86–98.
[9] J. Hu, Y. Zhou, C. Dalton, Effects of the corner radius on the near wake of a square prism, Experiments in fluids 40 (1) (2006) 106–118.
[10] H. Bai, M. M. Alam, Dependence of square cylinder wake on reynolds number, Physics of Fluids 30 (1) (2018) 015102.
[11] H. A. Khaledi, H. I. Andersson, On vortex shedding from a hexagonal cylinder, Physics Letters A 375 (45) (2011) 4007–4021.
[12] Z. W. Tian, Z. N. Wu, A study of two-dimensional flow past regular polygons via conformal mapping, Journal of fluid mechanics 628 (2009) 121–154.
[13] U. Fey, M. König, H. Eckelmann, A new Strouhal-Reynolds-number relationship for the circular cylinder in the range $47 < Re < 2 \times 10^5$, Physics of Fluids 10 (7) (1998) 1547–1549.
[14] X. Yang, Z. Yan, Y.-B. Yang, L. Wang, S. Zhao, Study on the drag reduction and vortex-induced vibration of an 18-sided polygon cylinder, Ocean Engineering 295 (2024) 116961.
[15] Q. Wang, L. Gan, S. Xu, Y. Zhou, Vortex evolution in the near wake behind polygonal cylinders, Experimental Thermal and Fluid Science 110 (2020) 109940.
[16] E. Masoudi, D. Sims-Williams, L. Gan, Flow separation from polygonal cylinders in an incident flow, Physical Review Fluids (2023).
[17] B. Ahlborn, M. L. Seto, B. R. Noack, On drag, strouhal number and vortex-street structure, Fluid dynamics research 30 (6) (2002) 379.
[18] E. Masoudi, Flow around stationary and oscillating polygonal cylinders, Ph.D. thesis, Durham University, unpublished thesis (2023).
[19] M. Breuer, G. De Nayer, M. Münsch, T. Gallinger, R. Wüchner, Fluid–structure interaction using a partitioned semi-implicit predictor–corrector coupling scheme for the application of large-eddy simulation, Journal of Fluids and Structures 29 (2012) 107–130.
[20] S. Atluri, V. Rao, C. Dalton, A numerical investigation of the near-wake structure in the variable frequency forced oscillation of a circular cylinder, Journal of Fluids and Structures 25 (2) (2009) 229–244.
[21] E. R. Van Driest, On turbulent flow near a wall, Journal of the aeronautical sciences 23 (11) (1956) 1007–1011.
[22] J. L. Lumley, The structure of inhomogeneous turbulent flows, Atmospheric turbulence and radio wave propagation (1967).
[23] H. Wang, Q. Gao, L. Feng, R. Wei, J. Wang, Proper orthogonal decomposition based outlier correction for piv data, Experiments in fluids 56 (2) (2015) 1–15.
[24] L.-H. Feng, J.-J. Wang, C. Pan, Proper orthogonal decomposition analysis of vortex dynamics of a circular cylinder under synthetic jet control, Physics of Fluids 23 (1) (2011) 014106.
[25] S. Gordeyev, F. O. Thomas, Coherent structure in the turbulent planar jet. part 2. structural topology via pod eigenmode projection, Journal of Fluid Mechanics 460 (2002) 349–380.
[26] R. Perrin, M. Braza, E. Cid, S. Cazin, A. Barthet, A. Sevrain, C. Mockett, F. Thiele, Obtaining phase averaged turbulence properties in the near wake of a circular cylinder at high reynolds number using pod, Experiments in Fluids 43 (2007) 341–355.
[27] L. Sirovich, Turbulence and the dynamics of coherent structures., Quarterly of applied mathematics 45 (3) (1987) 561–590.
[28] M. Stöhr, R. Sadanandan, W. Meier, Phase-resolved characterization of vortex–flame interaction in a turbulent swirl flame, Experiments in fluids 51 (4) (2011) 1153–1167.
[29] B. Cantwell, D. Coles, An experimental study of entrainment and transport in the turbulent near wake of a circular cylinder, Journal of fluid mechanics 136 (1983) 321–374.
[30] J. Sung, J. Yoo, Near-wake vortex motions behind a circular cylinder at low reynolds number, Journal of fluids and structures 17 (2) (2003) 261–274.
[31] J. C. Hunt, A. A. Wray, P. Moin, Eddies, streams, and convergence zones in turbulent flows, Studying turbulence using numerical simulation databases, 2. Proceedings of the 1988 summer program (1988).
[32] G. Birkhoff, E. Zarantonello, Jets, Wake and Cavities, Academic Press, New York, 1957.
[33] E. Berger, R. Wille, Periodic flow phenomena, Annual Review of Fluid Mechanics 4 (1) (1972) 313–340.
[34] J. W. Schaefer, S. Eskinazi, An analysis of the vortex street generated in a viscous fluid, Journal of Fluid Mechanics 6 (2) (1959) 241–260.
[35] G. Koopmann, The vortex wakes of vibrating cylinders at low reynolds numbers, Journal of Fluid Mechanics 28 (3) (1967) 501–512.
[36] E. Berger, Die bestimmung der hydrodynamischen größen einer kármánschen wirbelstraße aus hitzdrahtmessungen bei kleinen reynoldsschen zahlen:(gekürzte fassg.), Ph.D. thesis (1963).

[37] O. M. Griffin, S. E. Ramberg, On vortex strength and drag in bluff-body wakes, Journal of Fluid Mechanics 69 (4) (1975) 721–728.
[38] O. M. Griffin, S. E. Ramberg, The vortex-street wakes of vibrating cylinders, Journal of Fluid Mechanics 66 (3) (1974) 553–576.
[39] Y. Zhou, R. Antonia, A study of turbulent vortices in the near wake of a cylinder, Journal of Fluid Mechanics 253 (1993) 643–661.
[40] P. G. Saffman, Vortex dynamics, Cambridge university press, 1995.
[41] M. M. Alam, Y. Zhou, Alternative drag coefficient in the wake of an isolated bluff body, Physical Review E 78 (3) (2008) 036320.
[42] S. F. Hoerner, Fluid-dynamic drag, practical information on aerodynamic drag and hydrodynamic resistance, Fluid-Dynamic Drag pp. (1965) 0–2, 2–8.